



Comparative study on dielectric and structural properties of undoped, Mn-doped, and Ni-doped ZnO nanoparticles by impedance spectroscopy analysis

P. Norouzzadeh¹ · Kh. Mabhouti¹ · M. M. Golzan¹ · R. Naderali¹

Received: 28 July 2019 / Accepted: 4 November 2019 / Published online: 13 November 2019
© Springer Science+Business Media, LLC, part of Springer Nature 2019

Abstract

In this work, the results of the structural and dielectric investigation of pure, Mn-doped, and Ni-doped ZnO nanoparticles (NP_s), which have been prepared by simple sol–gel method using zinc acetate as precursor, are studied. The synthesized samples are examined via XRD at 300 K, FE-SEM, FTIR, and μ Autolab/FRA2 impedance spectroscopy techniques. XRD results and calculated lattice parameters of all synthesized samples have revealed that diffraction peaks are well matched to the JCPDS card No. 036-1451. FE-SEM obtained images confirm the formation of NP_s. The FTIR graphs exhibit the characteristics transmittance peaks at 510.01 cm⁻¹, 514.36 cm⁻¹, and 509.43 cm⁻¹ for pure, Mn-doped, and Ni-doped ZnO, respectively. This technique also authenticates the existence of ZnO NP_s and doped ones. The dielectric measurements of all synthesized samples have been done in the ranges of 10⁻³ to 10⁶ Hz. Dielectric investigations reveal that the size of the NP_s and dopant type have a great effect on the dielectric manner of samples. The obtained experimental results exhibit that the dielectric constant, loss tangent, electric modulus, and AC electrical conductivity parameters have intense frequency dependence. AC conductivity increases with frequency increment but decreases with doping, making it a potential option for device applications. In principle, an increment in capacitance and dielectric constants values has caused a decrement in frequency, while on the contrary, frequency increasing exhibits an increment of the AC electrical conductivity and electric modulus values. Finally, the magnetic studies extracted from electrical measurement are investigated.

1 Introduction

In the recent years, metal oxide nanomaterials have gained a great attention because of their size- and dopant-dependent structural and electrical properties and also due to their application as gas sensors [1], light emitting diodes (LEDs) [2], and varistors [3]. Among the metal oxide nanomaterials, the II-VI compound zinc oxide (ZnO) is one of the important and adaptable n-type material compared to other ones, which possesses interesting properties such as wide direct band gap equal to 3.37 eV [4]. ZnO has some significant advantages such as inexpensive, abundance in nature, easy fabrication, nontoxicity, and good chemical and mechanical stability [5]. Furthermore, it has high photoelectric coupling ratio which leads to great photoelectric properties, low

dielectric constant, and ultrahigh-frequency electroacoustic transducers caused by piezoelectric properties which results from low conductivity [6, 7]. Actually the basic dielectric properties of ZnO NP_s will be controlled and also modified by various dopants [8] hence, to use ZnO nanomaterials in different application fields, it is doped by various selective metal ions. Formation of defects and distortion in the ZnO lattice through doping with transition metals (TM_s) like Co, Mn, Cr, and Ni [9–11] considerably modifies the electrical properties of ZnO-based nanomaterials [12]. According to Zia et al.'s [13] investigations on the cobalt-doped ZnO nanostructures, increment of defects like zinc interstitials (Zni) and oxygen vacancies (Vo) through doping lead to low conductivity. Among the TM_s doping elements, the usage of Mn and Ni into the ZnO structure, because of their unique properties, has been prominent in the recent years [14, 15]. One of the major reasons for using these elements as dopants is comparable ionic radius of each element (Ni²⁺ = 0.069 nm and Mn²⁺ = 0.066 nm) with Zn²⁺ (0.074 nm), which makes it easy for Ni²⁺ and Mn²⁺ sub-lattices to replace Zn²⁺ in ZnO lattice [16, 17]. Studying the material's dielectric behavior

✉ Kh. Mabhouti
kh.mabhouti@urmia.ac.ir

¹ Department of Physics, Faculty of Sciences, Urmia University, Urmia, Iran

as an important physical property is necessary. In order to examine the dielectric properties of nanomaterial, Impedance spectroscopy (IS) as a formidable method has been utilized with the application of different frequencies. Investigations of the electrical properties and AC conductivity of the nanomaterials could help to understand the conduction mechanism and defects states which exist in the materials. To the best of our knowledge, despite some study about the dielectric and structural properties of ZnO nanoparticles, papers devoted solely to a systematic description of the optoelectrical efficiency through the impedance spectroscopy analysis techniques of semiconductor nanomaterials have seldom been reported specially about the magnetic properties (complex magnetic permeability and magnetic loss tangent) which extracted from electrical data are also investigated in this frequency range. Also, the relationships between the variation in impedance and capacitance of pure, Mn-doped and Ni-doped ZnO NP_s as a function of frequency variations. Actually, in this work, we selected two practical metallic ions with approximately opposite magnetic properties and also comparable ionic radius as dopants in a well-known host matrix named ZnO, with equal molarity and similar synthesize conditions which causes different morphologies like nanoparticles or some nanorod-like shapes and investigated the effects of these types of morphologies on the electrical and extracted magnetic properties of synthesized samples. Numerous chemical methods like hydrothermal [18], sol–gel process [19], co-precipitation [20], solvothermal [21], and spray pyrolysis [22] have been utilized to synthesize ZnO NP_s. In comparison with other synthesized routes, sol–gel is commonly used to preparation ZnO NP_s due to its environment friendly and low cost. In the present work, the sol–gel synthesized ZnO NP_s have been investigated with the help of X-ray diffractometer (XRD), field emission scanning electron microscopy (FE-SEM), Fourier-transform infrared (FTIR) spectroscopy, and impedance spectroscopy (IS).

2 Experimental

2.1 Sample preparation

Pure, Ni-doped, and Mn-doped ZnO NP_s are prepared by simple sol–gel method using highly pure of Zinc acetate dehydrate (ZAD) as the precursor, Manganese (II) acetate tetrahydrate, and Nickel nitrate hexahydrate as dopants, 2-methoxyethanol as solvent, and monoethanolamine (MEA) as a stabilizer. All the reagents in this experiment are of analytical grade and purchased from Merck. To prepare undoped ZnO, ZAD is dissolved in 2-methoxyethanol and stirred at 60 °C for 30 min. The concentration of ZAD is kept at 0.75 M. After that, the MEA is added dropwise into the solution during the stirring.

The molar ratio of ZAD to MEA is kept at 1.0. The resultant product is stirred for 90 min at the same temperature until a homogeneous solution is formed. The final solution is aged at a room temperature for a day and then put in the furnace (Exciton EX.1200-2L), the temperature is raised progressively up to 500 °C in the rate of 5 °C/min then kept at the same temperature for 1 h. Finally, the sample is left to cool down. Similar procedure has been adopted to prepare Mn-doped and Ni-doped ZnO NP_s except after the step of adding MEA, Manganese (II) acetate tetrahydrate, and nickel nitrate hexahydrate as doping materials are added to each product and the final product is stirred for 90 min at the same condition until a clear and homogeneous solution is formed. In the doped solutions prepared above, the required amount of Manganese (II) acetate tetrahydrate and Nickel nitrate hexahydrate with Mn/Zn and Ni/Zn atomic ratio of 5% is added to obtain MZO and NZO solutions. Actually, the main goal in the present work is just to study the influence of two different practical magnetic ions as dopants in the ZnO lattice at the same conditions (same synthesis process and the same molarity). Finally, ZnO nanopowders are compacted into a disk shape form of 31.28 mm in diameter and 1.98 mm thickness under a uniaxial pressure of 110 MPa and then sandwiched between the two highly pure copper disk-shaped metal foils to give a Cu/nano-ZnO/Cu double junction system as a parallel-plate capacitor. The same process is done for other samples under a uniaxial pressure of 120 and 150 MPa for Ni-doped ZnO and Mn-doped ZnO nanopowders, respectively [23]. The mentioned pressures for compacting the powders are obtained by performing multiple tests and finally the best pressure is selected, where the pellets were without cracking. The compaction of these powders into a disk shape gives them the properties of pellet or thick film as their thickness is in excess of one micron [24].

2.2 Measurements

The crystal structure and crystalline size of synthesized samples are done by using high-resolution XRD (Philips PW 1730) provided with Cu-K_α radiation at $\lambda = 0.154056$ nm from an angle $2\theta = 10^\circ - 80^\circ$. The surface morphology of all synthesized samples is examined via FE-SEM (MIRA3, Tescan, Czech Republic). Chemical bonding presents are examined by FTIR (Thermo scientific, Nicolet Avatar, USA) over a frequency range of 4000–400 cm⁻¹. Impedance Measurements are carried out with the help of μ Autolab Fra2 through a frequency range of 10⁻³ Hz to 10⁶ Hz.

3 Results and discussion

3.1 XRD analysis

Figure 1 indicates XRD patterns of prepared nanopowders. As it can be seen, each sample well matches with the standard pattern of JCPDS card No. 036-1451, also we can deduce that XRD peaks are crystallized in a wurtzite hexagonal structure. There are not any additional peaks in the patterns of pure and Mn-doped ZnO. The patterns confirm that Mn^{2+} successfully replaces the ZnO lattice at the Zn^{2+} site. However, the weak extra peaks proportional to a secondary phase are revealed as Ni doping percentage over 4% which verifies the replacement limit for Ni doping into ZnO lattice sites. The replacement limit of Ni^{2+} doping percentage into ZnO lattice has also been published by Liu et al. [25]. Figure 2 exhibits that centers of the major peaks are slightly shifted and also diffraction peaks intensities are a little different from each other which could be assigned to the ionic radii differences. The lattice parameters c and a for the hexagonal structure are obtained from the (002) and (100) peaks, respectively, which are shown in Table 1. Compared to our results, it can be observed that hcp phase is formed in our sample and the obtained trivial variation in the synthesized samples may be attributed to the nanometric features of the crystallites and defects. According to the literature [26, 27], the mean crystallite diameters of NP_s are computed using peaks broadening with the help of the X'Pert HighScore software and the common Debye–Scherrer method as follows [28]:

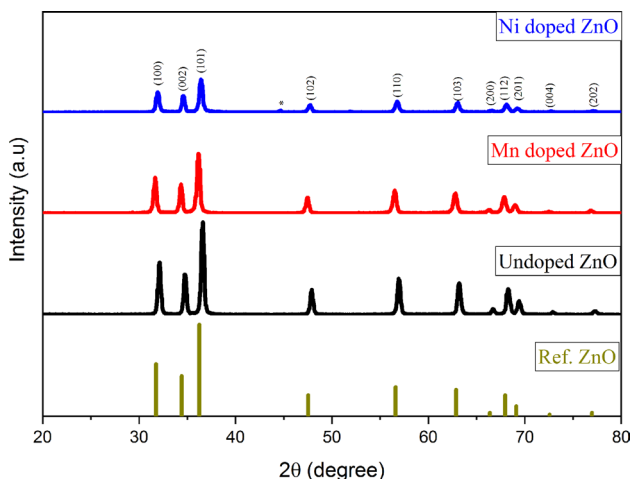


Fig. 1 X-ray diffraction (XRD) patterns of synthesized undoped, Mn-doped, and Ni-doped ZnO nanopowders and the standard ZnO (JCPDS card No. 036-1451)

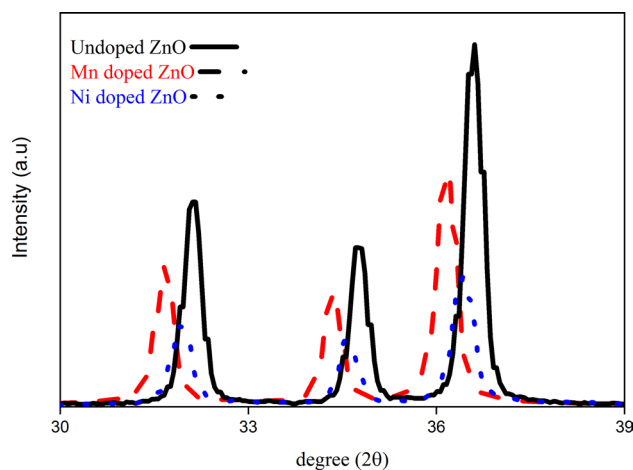


Fig. 2 Comparing three major XRD patterns of synthesized undoped, Mn-doped, and Ni-doped ZnO nanopowders

$$D = \frac{k\lambda}{\beta_{hkl} \cos \theta}, \quad (1)$$

where D is the crystallite diameter, k equals to 0.9, β is the full width at half maximum (FWHM), and θ is the corresponding Bragg's angle.

The calculated average grain sizes of the samples are 26.76 nm, 24.88 nm, and 23.58 nm for pure, Mn-doped, and Ni-doped ZnO, respectively.

3.2 Morphological studies

The surface morphology of the synthesized NP_s are examined using FE-SEM. The obtained images are depicted in Fig. 3a–c. In order to determine the diameter of the synthesized particles from FE-SEM images, Digimizer 4.1.1.0 [29] and Image J [30] as two common image analysis software are used. As it can be seen in Fig. 3a, undoped ZnO NP_s are distributed in a random manner and have different sizes. The average particle size is found about 70 nm, with a maximum of 133 nm and a minimum of 20 nm for the amount of 50 NP_s . Figure 3b exhibits the Mn-doped ZnO NP_s , we can observe that there are two types of particles, some of them are with the mean size of about 35 nm and

Table 1 Lattice parameters (a and c) and cell volume (V) of all synthesized samples

Samples	a (Å)	c (Å)	c/a	V (Å ³)	Structure
JCPDS 36-1451	3.2498	5.2066	1.602	47.62	Hexagonal
Undoped ZnO	3.2135	5.1587	1.605	46.13	Hexagonal
Mn-doped ZnO	3.2546	5.2231	1.604	47.91	Hexagonal
Ni-doped ZnO	3.2283	5.1829	1.605	46.77	Hexagonal

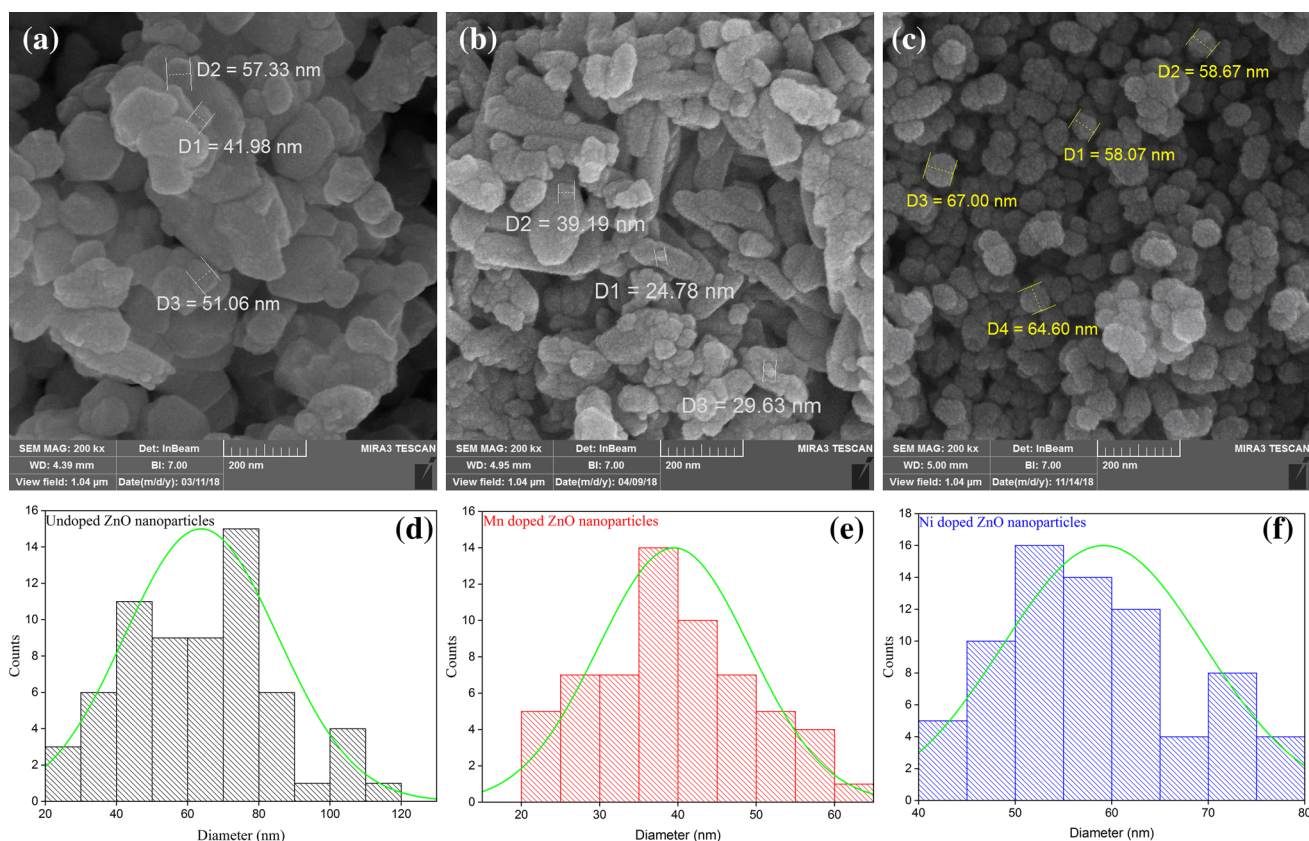


Fig. 3 FE-SEM images of **a** undoped ZnO NP_s; **b** Mn-doped ZnO NP_s; **c** Ni-doped ZnO NP_s and size distribution of the synthesized NP_s for **d** undoped ZnO; **e** Mn-doped ZnO; **f** Ni-doped ZnO NP_s

some others are rod-like. Many rod-like hexagonal structures can be obviously seen. The diameter grown as Mn-doped ZnO nanorods is in the range of ~30 to 100 nm and the length varies from ~100 to 300 nm. The hexagonal nuclei are initially constituted because pure ZnO has a hexagonal structure. Since Mn has a cubic crystal structure, the hexagonal boundaries of the grains structure are progressively deteriorated and slowly vanished by substitution of Mn ions into the ZnO lattice structure and become a rod-like structure in random orientations. We can deduce that the substitution of Mn ions into ZnO lattice significantly affect the size and shape of the ZnO nanopowders [17]. The FE-SEM image of Ni-doped ZnO sample in Fig. 3c indicates that the grain sizes are ranged from 48 to 80 nm. The average particle size is found about 61 nm, for the amount of 25 NP_s. The high magnification FE-SEM images indicate that the NP_s seems to be in the form of hexagonal and spherical structure with smaller grain size compared to the pure ZnO. For Ni-doped ZnO sample, particle size is decreased since concentration of Ni²⁺ is approximately 5–15%. Actually, the existence of defects such as Ni interstitials could be the reason of particle size decreasing as Ni doping. Also, this sample demonstrates a few of agglomeration which may be attributed to the

attractive forces presence between NP_s due to an increase in surface area-to-volume ratio [31]. We suggest that metal ions change the surface form of the ZnO NP_s, the crystal size, and the mechanism of aggregation of NP_s. Therefore, the FE-SEM images imply that ion incorporation is one of the factors affecting the surface morphology [32]. We can deduce from all the graphs that, the grain sizes of the prepared samples verify that all the synthesized samples are in nano range, which are in well consent with the calculated particle size from the XRD method. Crystallite sizes obtained from FE-SEM are slightly higher than those crystallite size values calculated from XRD data. This observed variation is probably due to surface structure of coalescence grains leading to higher grain growth which brings out porosity and surface roughness [33]. The size distribution histograms of undoped, Mn-doped, and Ni-doped ZnO NP_s are presented in Fig. 3d, e, and f, respectively.

3.3 Fourier-transform infrared spectroscopy study

The chemical bonding, composition, and molecular structure in a material can be analyzed using FTIR. This technique was utilized to investigate the functional groups of the

synthesized NP_s. FTIR spectra are measured in the ranges between 400 and 4000 cm⁻¹ and presented in Fig. 4a. The synthesized NP_s FTIR peaks and their assignments are indicated in Table 2, which are in well agreement with the previous studies [34–39]. Through doping, vibrational frequencies changed are caused by the bond lengths differences. As a result, the alteration in the peak position of ZnO bands indicates that ZnO lattice is interrupted by the existence of

Mn²⁺ and Ni²⁺ in its background and these ions are replaced in the ZnO lattice sites and cause stretching or bending. <https://www.nature.com/articles/srep27689-ref60> It can thus be mentioned that FTIR spectroscopy is in well agreement with the obtained XRD data. The position of peaks exhibits a slight shift which may be related to the defects encircling Ni and Mn ions in the ZnO matrix causing anti-bonding or disorder. Also, this slight shift can be related to the differences in ionic radii of Zn and Ni or Mn, and bond length differences originate from structural modifications because of doping, which is another reason that verifies the replacement of Ni and Mn ions into the ZnO lattice [40]. As a result, doping can affect FTIR spectra peaks, hence in Fig. 4b, a large view of the FTIR spectra in the ranges 400–700 cm⁻¹ is provided. As it can be seen, the undoped ZnO plot indicates a slight shift to the lower and higher wavenumbers through doping, also variation in the position of the observed peak for undoped ZnO sample, in the Mn-doped ZnO sample is noticeable compared to Ni-doped ZnO sample.

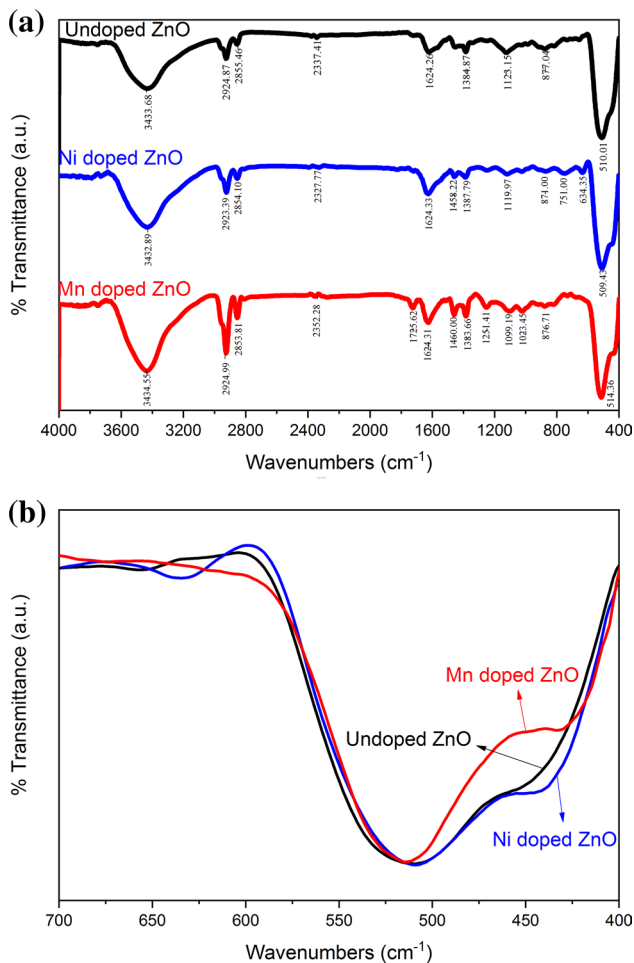


Fig. 4 a FTIR spectra of undoped, Mn-doped, and Ni-doped ZnO NP_s and b a large view of the FTIR spectra for the synthesized NP_s in the ranges 400–700 cm⁻¹

Table 2 IR peaks and their assignments for the synthesized undoped, Mn-doped, and Ni-doped ZnO NP_s

Assignments	Wave number (cm ⁻¹)		
	Undoped ZnO	Mn-doped ZnO	Ni-doped ZnO
O–H stretching	3433.68	3434.55	3432.89
C–H stretching	2924.87	2924.99	2923.39
CO ₂ asymmetric stretching	2337.41	2352.28	2327.77
H–O–H bending vibration	1624.26	1624.31	1624.33
Zn–O stretching (metal oxide vibration)	510.01	514.36	509.43

3.4 Impedance analysis

The dielectric nature of pure, Ni-doped, and Mn-doped ZnO NP_s at 300 K are studied with the help of impedance data from μ Autolab/FRA2 in the frequency range between 10⁻³ and 10⁶ Hz. Some parameters like capacitance, AC conductivity, loss tangent, dielectric constant, and modulus are studied. The Nyquist plot which indicates complex impedance Z'' (imaginary part) against Z' (real part) is depicted in Fig. 5a–c for pure, Mn-doped, and Ni-doped ZnO NP_s, respectively. As it can be seen, the horizontal and vertical values of the graphs are not the same which attributed to this reason that samples with different doping ions may exhibit semicircular patterns in their own specific horizontal and vertical values (not the same ones) [41]. In Fig. 5, compared with pure and Mn-doped ZnO NP_s, Ni-doped ZnO NP_s indicate the arc with bigger diameter which verifies lower performance of charge transfer [42]. The frequency dependent of impedance for all synthesized NP_s is shown in Fig. 6. It can be seen that for all samples, impedance decreases with frequency increasing which could be caused by a significant

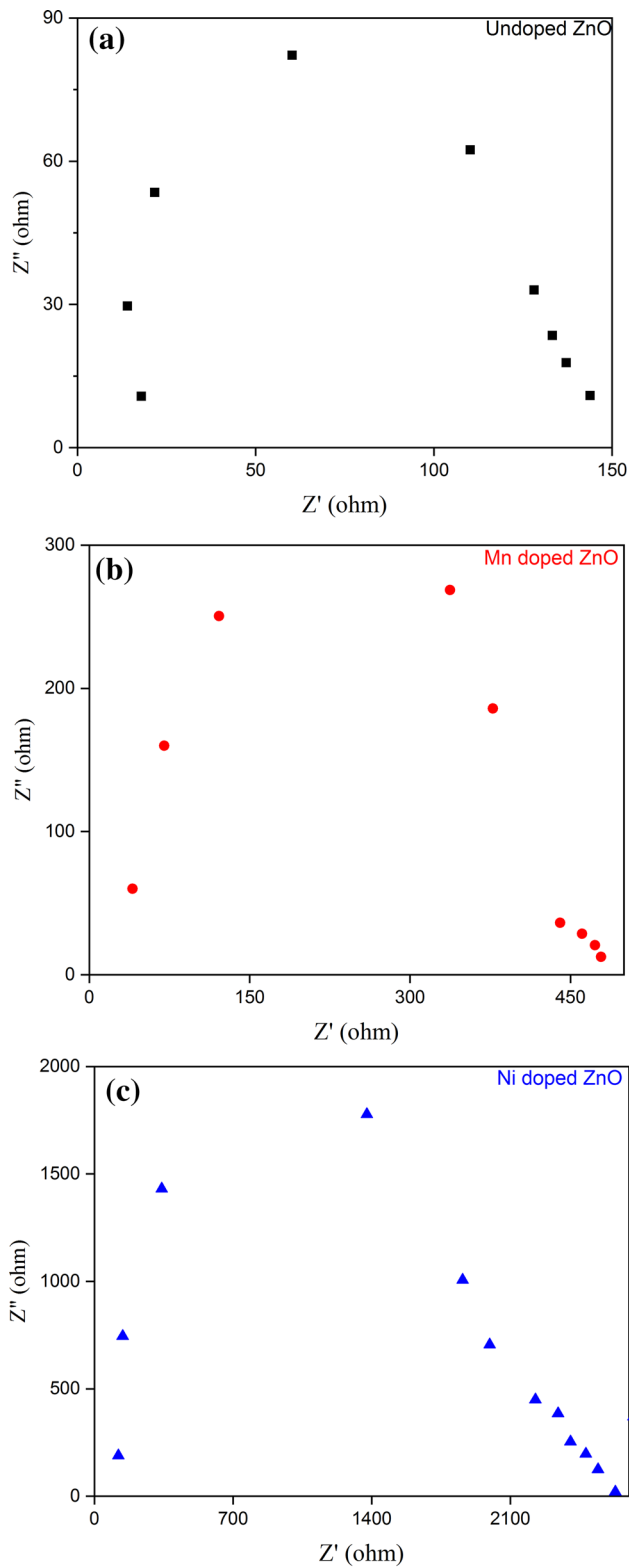


Fig. 5 Nyquist plot between a real impedance (Z') and imaginary impedance (Z'') of **a** pure ZnO; **b** Mn-doped; and **c** Ni-doped ZnO NP_s

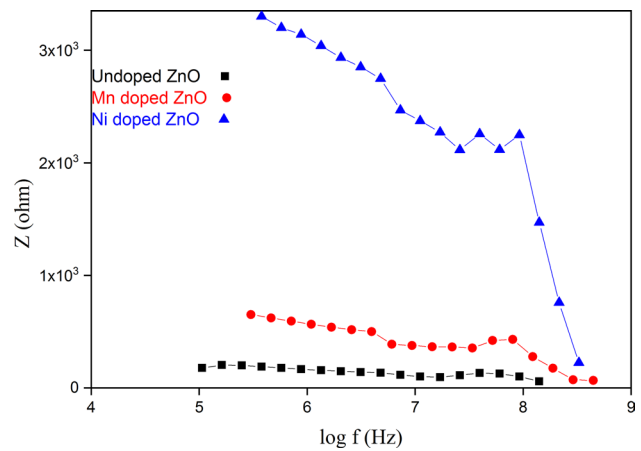


Fig. 6 Frequency-dependent variation in impedance for pure and doped ZnO NP_s

role of grain boundaries of ZnO lattice. Furthermore, ZnO shows lower impedance relative to Mn-doped and Ni-doped ZnO NP_s. We can deduce that impedance could be modified by various dopants. Generally in high-frequency region, the grains are effective while the grain boundaries are effective in low-frequency region. Semicircle shows grain contribution in the low-frequency region that corresponds to the grain boundary contribution representing bulk properties of material [43]. The electrical characteristic of a material is exhibited by the appearance of semicircular arcs in Nyquist plots. It has been reported in literature that the resistivity of a material, in general increases with the decrease in grain size [44, 45]. Figure 6 shows the frequency-dependent variation in impedance (Z) with real part (Z') and reactive part (Z''). The impedance Z decreases with increase in frequency for Ni-doped and Mn-doped samples resulting from the hopping phenomenon. Z' has strong frequency dependence in the lower frequency region which is due to the effectiveness of resistive grain boundaries in this region. The reactive part of impedance Z'' has a similar behavior as Z' , however, Z'' causes to the decrease in capacitance. In Fig. 5a–c, the capacitive and resistive components of data are plotted in a complex plane plot, it appears in the form of sequence of semicircles representing electrical phenomenon due to the bulk grain material, grain boundary, and interfacial phenomenon. In Ni-doped sample, the presence of Ni ions and defects such as surface defects (Zn_i), singly ionized oxygen vacancy state (O_v), and antisite oxygen-related defect states (O_{Zn}) lead to an increase in dipole moment adding to the effect of correlated barrier hopping between different metal ions (Zn^{4+} , Zn^{2+} , Ni^{3+} , Ni^{4+}). Electrical conductivity elucidates the semiconductor behavior of these 3d transition metal (Ni) with conductivity which depends on the increase in nickel doping in ZnO at room temperature.

Complex impedance spectra demonstrate the existence of semicircle suggesting the dominance of grain boundary resistance in the Ni-doped samples as shown in Fig. 6.

Figure 7 depicts the measured capacitance of synthesized NP_s as a function of frequency. Complex impedance and capacitance can be linked together by the following relation:

$$C = \frac{1}{2\pi f Z''} \tag{2}$$

Capacitance results are extracted from the Z measurements using Eq. 2 since impedance spectroscopy measurements give us the Z, Z', and Z'' values at specific frequencies, and then we can use Eq. 2 to calculate capacitance values. As shown in Fig. 7, the capacitance of all samples reveals a nonlinear manner and decreases with frequency increasing which may be relevant to the presence of traps. Charges with various time constants will be induced by various types of traps and forcefully adjust capacitor charges at specific frequencies. Higher capacitance values deduce at low frequencies where induced charges are adaptable to ac signal, inversely, at high frequencies, charges are not able to respond to the voltage. High Capacitance values at lower frequencies could be ascribed to the barrier-blocked charges. These phenomena could also be explained by dielectric materials features where applying field may affect charge carriers movements due to the presence of impedance in charge carriers movements path and space charges polarization [23, 46]. The obtained capacitance values of samples are varied approximately from 200 nF to 8 × 10⁸ nF, from 2 nF to 6 × 10⁷ nF, and 1.5 nF to 3 × 10⁸ nF for pure, Ni-doped and Mn-doped ZnO, respectively. The results of capacitance, grain sizes, and ionic radius of all synthesized NP_s are exhibited and compared in Table 3. The mentioned value for capacitance, 10⁸ nF (= 0.1 F), is a usual value in

Table 3 Capacitance (C_F), grain sizes (D), and ionic radius (r) of synthesized NP_s

Sample	C _F (nF)	D (nm)	r (nm)
Undoped ZnO	200	26.76	0.074
Mn-doped ZnO	1.5	24.88	0.066
Ni-doped ZnO	2	23.58	0.069

this type of experiments and measurements. Since our measurements are done at the zero voltage, it is in a good consent with literature [47].

The dielectric constant measurement is related to the stored charges. Actually, real part is relevant to energy storage, while imaginary part is associated with inducing energy losses [48]. The relationships of the dielectric constants can be expressed as follows [49]:

$$\epsilon' = \frac{z''}{\omega C_0(z'^2 + z''^2)} \tag{3}$$

$$\epsilon'' = \frac{z'}{\omega C_0(z'^2 + z''^2)} \tag{4}$$

The graphs of the real and imaginary parts of dielectric constant versus frequency for all synthesized NP_s are depicted in Figs. 8 and 9. According to Fig. 8, the dielectric constant increases by decreasing frequency due to a relaxation phenomenon that is specified by the greatest dielectric loss [47]. It may be deduced from scattering of charge carriers or rapid change of electric field. This phenomenon also can be explained by Maxwell–Wagner (M–W) mechanism. Based on M–W mechanism, a nanomaterial is supposed to be comprised of good conducting particles which are segregated by poor conducting ones. By applying external electrical field, charge carriers can bring the grain boundaries

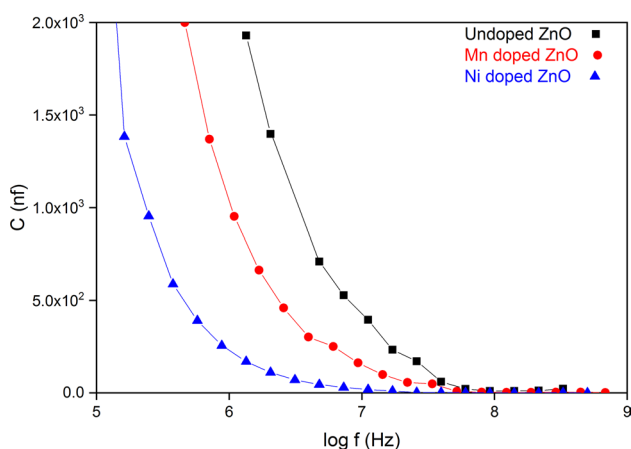


Fig. 7 Capacitance of pure, Mn-, and Ni-doped ZnO NP_s as a function of frequency

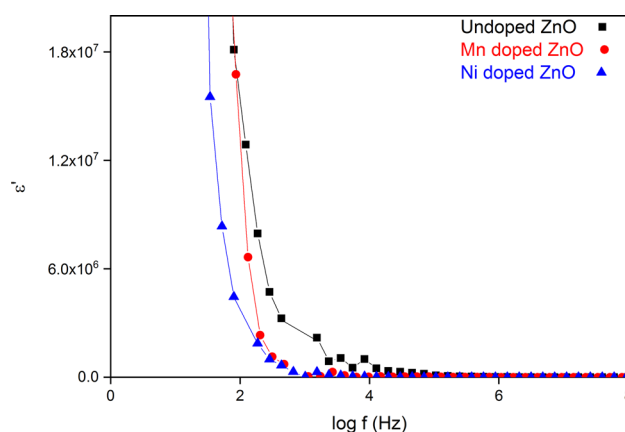


Fig. 8 Real dielectric constant as a function of frequency for undoped, Mn-, and Ni-doped ZnO NP_s

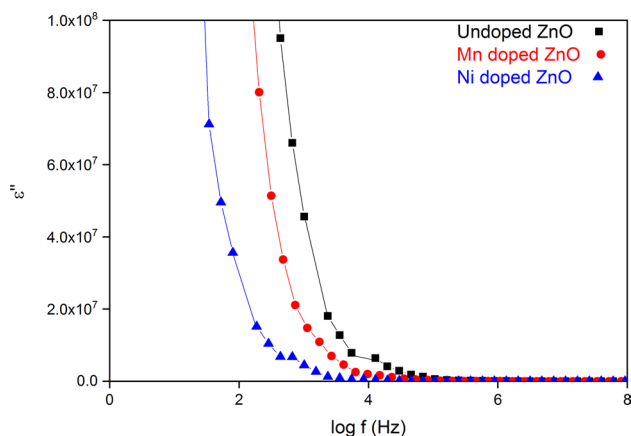


Fig. 9 Imaginary dielectric constant as a function of frequency for undoped, Mn-, and Ni-doped ZnO NP_s

together. Hence, presence of small polarization at high-frequency results in low dielectric constant. Dipoles oscillations will start to lay through the field when dipoles are not able to rotate rapidly enough for more time and consequently with adequate frequency increasing, dipoles will not be able to pursue the field and the direction of polarization vanishes; therefore they start to decrement and then receive a constant value. In principle, the charge carriers receive various resistances which lead to gathering of charges at different boundaries. This goes to an increment in the dielectric constant values [50, 51]. The maximum obtained values of real part of dielectric constant are 3.3×10^9 , 6×10^7 , and 3.9×10^9 for undoped, Ni-doped, and Mn-doped ZnO, respectively. Also for obtained maximum imaginary part, we have 2.05×10^{10} , 7.2×10^8 , and 1.3×10^{10} for undoped, Ni-doped, and Mn-doped ZnO, respectively. The frequency dependence of the imaginary part of the dielectric constant for all synthesized NP_s is illustrated in Fig. 9. As it can be seen, this part increases with the decreasing frequency, thus, at the lower frequency there is an inevitable polarization phenomenon and the conduction losses on the contrary high frequencies [52]. Taking everything into consideration, at the lower frequency, different types of polarization mechanisms such as ionic, surface, and dipolar polarizations cause different values of real and imaginary parts of dielectric constant. Actually, high values of dielectric constant associated to the conductivity of grain boundary at low frequencies [53]. As a result, at the low frequency, the undoped ZnO has the high dielectric constant values in comparison with doped samples. Also, the Mn-doped ZnO sample has larger dielectric constant compared with Ni-doped ZnO sample. The decrement in dielectric constant at the low frequency, according to various dopants, could be relevant to the mean particle sizes. In a dielectric material, the dielectric loss happens when electric polarization is not able to pursue the change

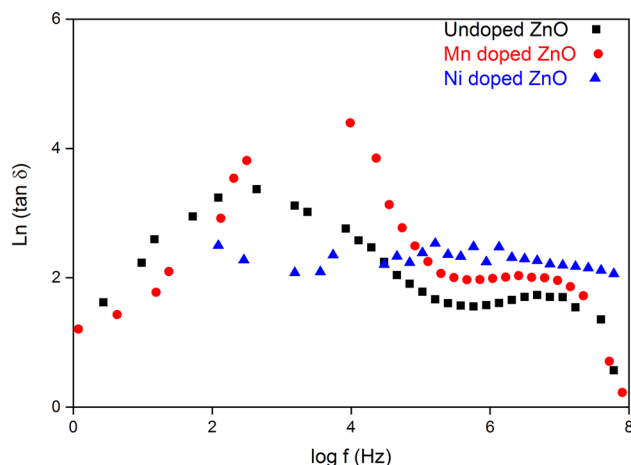


Fig. 10 Variation of dielectric loss with frequency of pure, Mn-, and Ni-doped ZnO NP_s

in the electric field. Actually, the dielectric loss arises when the polarization lags behind the applied alternating field and is caused by the impurities and imperfections in the crystal lattice [50]. Energy squandered in the dielectric system is studied in terms of dielectric loss tangent and can also be exhibited as follows [54]:

$$\tan \delta = \frac{\epsilon''}{\epsilon'} \quad (5)$$

The dielectric loss factor versus frequency plot is depicted in Fig. 10. As it can be seen, the dielectric loss slightly increases with decreasing the frequency of all synthesized NP_s which may be caused by space charge polarization. At lower frequencies, the dielectric loss is in its highest value for undoped sample and this parameter goes to decrement with the doping of Ni and Mn. As it is deduced, it is obvious that the Mn and Ni dopants progress the ZnO potential for high-frequency device usages [55]. Also, it seems that peaks shifted towards lower frequencies. This may be attributed to the existence of higher defects number in the nanopowders [56]. The decrease in loss tangent takes place when the jumping rate of charge carriers lags behind the alternating electric field beyond a certain critical frequency [57]. Each $\tan \delta$ plot demonstrates a relaxation peak revealing when frequency of the charge carriers gets nearly corresponding to the external electric field [58]. This manner also mentions the mediocre time used up via the charge carrier traps, which depends on the energy altering among the states. This energy difference will be changed by an applied field and thus a neat polarization will be produced which lags near the applied field due to the finite rates of the tunneling transition. This is a section of the polarization that is not in the same phase with the applied field and is named as the AC conductivity dielectric loss. The importance of AC conductivity studies in the dielectric materials attributes to the dynamic properties of these materials. Figure 11 exhibits the

dependence of the AC conductivity to the frequency at 300 K. It is obvious that the AC conductivity decreases with decreasing frequency for all samples. For a dielectric material, this parameter can be obtained as follows [59]:

$$\sigma_{ac} = \epsilon_0 \epsilon'' \omega \tag{6}$$

The main reason for AC conductivity increasing with frequency increment may be attributed to the charge carriers trapping in the samples. As it can be observed in Fig. 11, at low frequencies, increment is gradual, but it is faster at high frequencies. Existence of potential barrier at the lower frequency causes charge carriers not to be able to move among grain boundaries, but some of the carriers through the thermal excitation surmount the potential barrier and therefore produce a small conductivity. With increment of frequency, the thermal activation energy for tunneling increases conductivity. Consequently, at a specific frequency, charge carriers with adequate required energy could overcome the potential barrier and hence a quick increment of conductivity happens at a high frequency [58, 60]. Furthermore, Fig. 11 depicts that the AC conductivity of undoped ZnO NP_s is higher than Mn-doped and Ni-doped ZnO NP_s. Also, it can be deduced that Mn and Ni ions induce defects in the ZnO sites, like zinc interstitials (Zni) and Oxygen vacancies (Vos). This induced defects make the constitution of grain boundary defect barriers easy, therefore charge carriers flow get blocking which result in conductivity decrement. In a material, the electric modulus is defined as the relaxation through electric field when the electric replacement remains constant. Complex modulus is exhibited as follows:

$$M^* = M' + iM'' \tag{7}$$

$$M^* = 1/\epsilon^* = \frac{\epsilon'}{\epsilon'^2 + \epsilon''^2} + i \frac{\epsilon''}{\epsilon'^2 + \epsilon''^2} \tag{8}$$

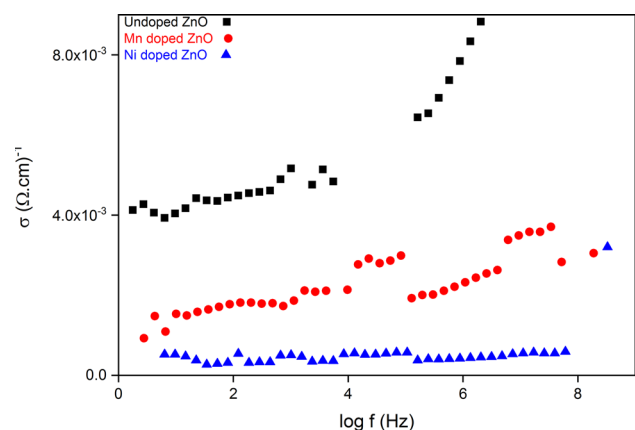


Fig. 11 AC conductivity as a function of frequency of pure, Mn-, and Ni-doped ZnO NP_s

The plots of frequency versus modulus for all synthesized samples are displayed in Figs. 12 and 13. As it can be seen, at high frequencies M' and M'' exhibit an increasing manner, but at the lower frequencies the amount of these parameters incline to get close to zero, indicating that we can ignore polarization part, and therefore charge carriers have ability to move in expanding range, this is also a confirmation of the removing electrical polarization contribution. As a result, ε' and ε'' increasing with frequency decreasing lead to an increment in the M' and M'' parameters. Finally, we can deduce that, at high frequency, the period is extremely lower than the lifetime of interface states. Consequently, the interface states are not able to pursue the AC signal, hence M' and M'' get to a maximum value, according to M_∞ = 1/ε_∞, because of the relaxation mechanism (Fig. 14). A comparative study reveals that the obtained data in present work are in a good agreement with previous works [41, 61, 62]. For

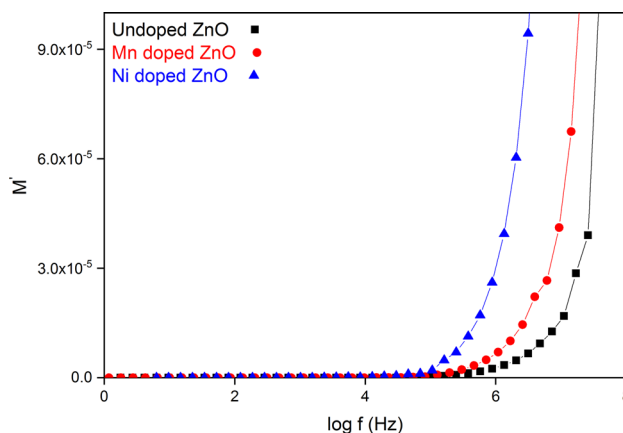


Fig. 12 Real part of modulus as a function of frequency of pure, Mn-, and Ni-doped ZnO NP_s

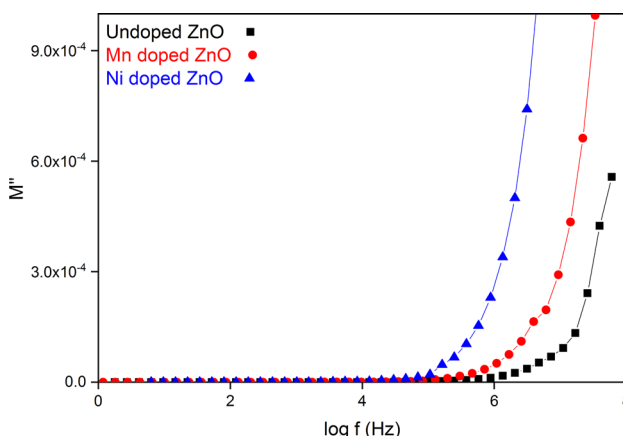


Fig. 13 Imaginary part of modulus as a function of frequency of pure, Mn-, and Ni-doped ZnO NP_s

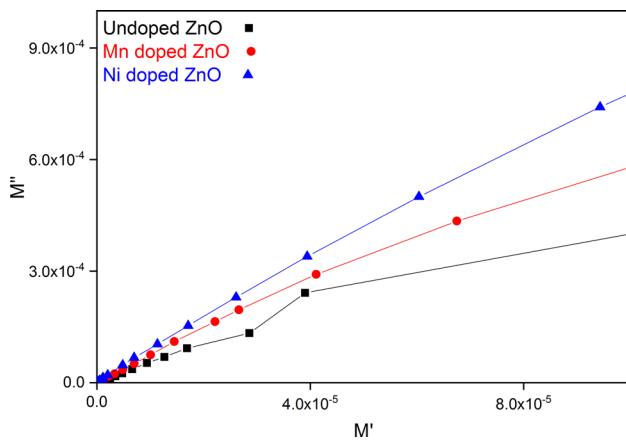


Fig. 14 Frequency Cole–Cole plots of pure and doped ZnO NP_s

example, as compared to Samanta et al. [41], the xrd results, also dielectric constant, loss tangent values, and general behavior of their plots are comparable and arguable with the mentioned work. Maximum calculated values of impedance, capacitance, dielectric constants, dielectric loss tangent, and AC conductivity in a specific frequency, which are presented in Figs. 6, 7, 8, 9, 10, 11, 12, and 13 are assortment in Table 4. As it can be seen from Table 4, maximum values of ac conductivity, capacitance, and imaginary part of dielectric constant parameters were decreased as Mn and Ni ions were present.

3.5 Magnetic studies (extracted from electrical measurements)

The magnetic permeability ($\mu = \mu' - j\mu''$) of the NPs could be obtained by measuring Z and ϵ , as follows [63]:

$$Z = \eta_0 \sqrt{\frac{\mu}{\epsilon}}, \quad (9)$$

where $\eta_0 (= 377\Omega)$ is the impedance characteristic of air.

Figure 15 shows the variations of real and imaginary parts of ($\mu = \mu' - j\mu''$) versus frequency. As shown in Fig. 15a, the value of the real part of μ is positive. This implies that there is a possibility of propagating magnetic field inside the material. The positive values of imaginary parts of μ

represent a magnetic loss, which is finally released from the magnetic loss conditions by increasing the frequency.

Figure 16 shows the magnetic loss tangent diagram. At first, by increasing frequency, its value is increased. Afterward, as illustrated, the maximum value of the loss tangent is observed at about the middle of the frequency range. The reduction of the loss tangent presents the weakly inductance behavior as the resistance behavior of the material is evaluated. Actually, with increasing frequency, magnetic loss tends to frequency-independent nature at a higher frequency. At high-frequency region, there may be some ionic vibration followed by space charge polarization leading to frequency-independent nature [58].

For more explanation, at first, NP_s experience change in the orientation of dipole polarization by means of the applied electric field. As a result, surface polar charges are generated and the accumulation of positive and negative charges characterizes capacitance behavior. As well known, the frequency is inversely proportional to the period of field fluctuation. This means that the field is applied to the NP_s in shorter time periods. Hence, the NP_s have less time to react to the applied field and change its dipole polarization orientation. Increasing the frequency leads to disturbing the arrangement of the orientation of the polarization and the distribution of surface polarized charges is consequently reduced. In other words, the dipoles have less time to rotate and change the polarization, so they could not reach the previous orientation. It is implied that the density of positive and negative charges accumulated within the NP_s and fundamentally, the capacitance would be reduced.

On the other hand, the existence of polarized charges at the surface leads to a distribution of surface currents. These surface currents can generate a magnetic field inside the NP_s. In the same way, magnetic dipoles are no longer being able to rotate in sufficient speed and thus they gradually lay behind the field. Therefore, same as to the permittivity curve (Fig. 8), the real and imaginary parts of μ decrease with the increase of the frequency. From Fig. 15a, b, it can be found that the permeability reaches its maximum value at the beginning of the frequency range. Moreover, as the frequency increases, the real and imaginary parts would be decreased. The existing defects such as vacancies in (Ni or Mn)-doped ZnO NP_s lead to the formation of a large number

Table 4 Obtained maximum values of impedance, loss tangent, dielectric constants, and ac conductivity at specific frequencies (f) which are indicated in Figs. 6, 7, 8, 9, 10, 11, 12, and 13

Samples	Z (ohm)	f (Hz)	10^{-8} C (nF)	f (Hz)	10^{-9} ϵ'	f (Hz)	10^{-10} ϵ''	f (Hz)	$\tan \delta$	f (Hz)	$\sigma_{ac}(\Omega.cm)^{-1}$	f (MHz)
Undoped ZnO	337.7	0.012	8.850	0.003	3.330	0.003	2.080	0.003	28.562	0.8680	0.223	1.000
Mn-doped ZnO	876.4	0.031	7.540	0.003	3.960	0.002	1.320	0.002	81.430	19.410	0.010	0.579
Ni-doped ZnO	4766.2	0.068	0.603	0.012	0.060	0.012	0.073	0.012	12.520	16.760	0.003	0.655

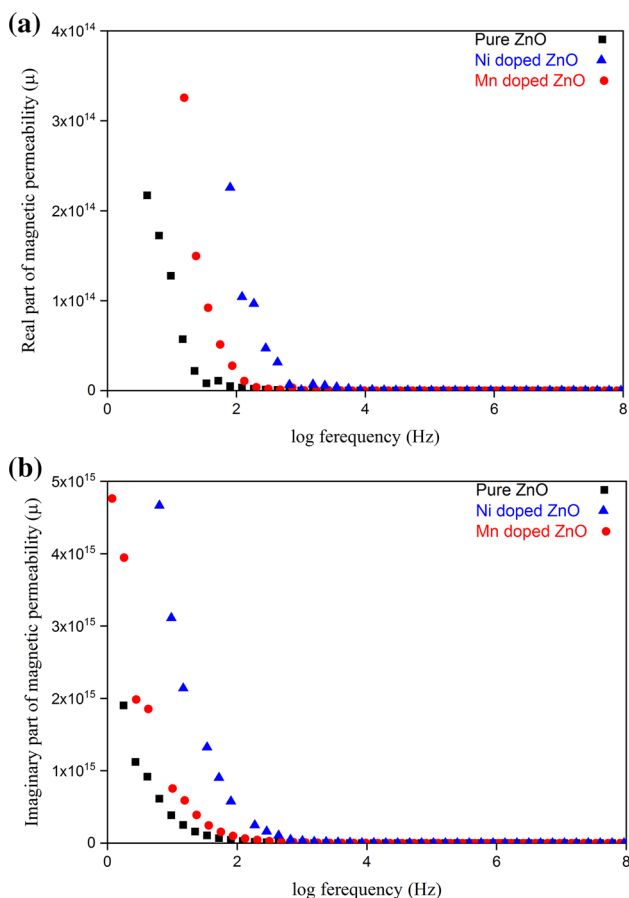


Fig. 15 a The real part and b the imaginary part of the magnetic permeability as a function of frequency for undoped, Mn-doped, and Ni-doped ZnO NP_s

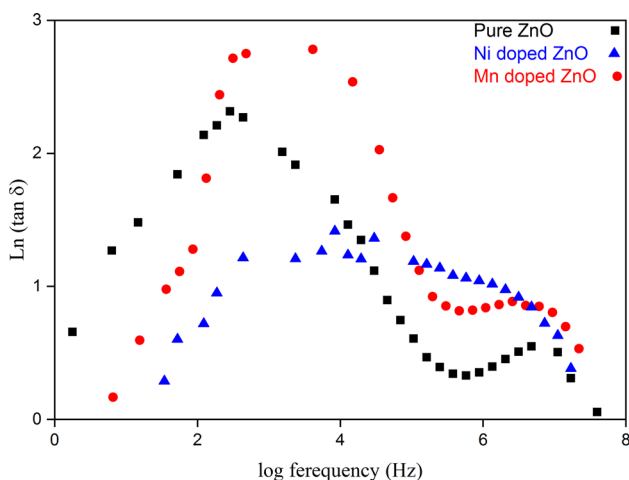


Fig. 16 Variation of magnetic loss with frequency for undoped, Mn-doped, and Ni-doped ZnO NP_s

of weakly bound ions and electric dipole moments (ion-vacancy pairs) [47].

Jaffe et al. [64] showed through electron paramagnetic resonance (EPR or ESR) that the EPR signal resulted from the O²⁻ deficiencies on the ZnO NP_s surface which can capture and trap electrons so that the paramagnetic resonance source with $S = 1/2$ is produced. Also, they showed that the photocatalytic activities of ZnO NP_s depended mainly on their surface properties such as area, oxygen deficiency, and hydroxyl attachments.

Diamagnetic to ferromagnetic change observed with increased concentration of nickel photoluminescence studies confirmed the presence of oxygen vacancy states (V_O) and zinc interstitials and ZnO ions (Zni) defects in the samples. It was concluded that the defect-induced strain, grain boundaries, and lower particle sizes are the reasons for weak ferromagnetic behavior of the investigated samples. An appropriate explanation for observed room temperature ferromagnetism (RTFM) [65] in Ni-doped sample is ferromagnetic exchange mechanism involving oxygen vacancies model. This is explained in terms of two reasons: first the number of oxygen vacancies (VO) and zinc interstitial (Zni), and second the exchange interaction between doped transition metal ion and O ion spins.

Thus, the magnetic coupling between Ni ions with ZnO is ferromagnetic mediated by V_{Zn} and V_O and this may account for the observed RTFM and indicates that defects play a role to get a ferromagnetic coupling. Further, in the present case for low magnetic field, the ferromagnetic behavior can be attributed to the presence of small magnetic dipole located at the surface of nanocrystals, which interact with their nearest neighbors inside the crystal involving oxygen vacancies.

Therefore, the proposed material experiences change in the orientation of dipole polarization by means of the external electric field. The existence of polarized charges leads to a distribution of displacement currents. Nevertheless, the movement of charge carriers within the grains would be easily possible due to the applied electric field, but the accumulation of the charge carriers on the grain boundary results in potential barriers. Hence, interfacial polarization could be implied. According to Fig. 8, the abrupt reduction in the real part of ϵ is observed. The abrupt decreasing of the real ϵ with increasing frequency is attributed to the barrier-blocked charge movement.

As shown in Fig. 11, the maximum value of the conductivity affirms the breaking of barrier-blocked charge. The more weakness of the magnetic behavior, the more amount of electric field energy is stored in the material and the capacitive behavior increases, simultaneously. This growth implies that the real part of permittivity is positive, and the possibility of propagation of the electric field is facilitated. As well as, according to the above-mentioned accumulation of the charges on the grain boundaries leads to capacitance

behavior. As the frequency increases, the traps of the charge carriers discharge into the adjacent low-sized particles. Thus, the conductivity could be increased which results in the magnetic behavior of the proposed material. According to the obtained results, it can be said that the priority and delay in the electrical and magnetic behavior of the NP_s versus the frequency domain depend on the doping.

4 Conclusion

In summary, pure, Ni-doped, and Mn-doped ZnO NPs have been prepared by a low-cost simple sol–gel route. Structural results verify the constitution of the ZnO hexagonal wurtzite structure in all samples and also all diffraction patterns are well indexed to the JCPDS card No. 036-1451. Differences in lattice parameters of synthesized samples revealed the replacement of Ni and Mn within the ZnO matrix. Among all synthesized samples, doped NPs exhibit better lattice parameters compared with the undoped ones. Actually, the lattice parameters in Mn-doped ZnO are more similar to JCPDS rather than undoped and Ni-doped ZnO NPs. The high magnification FE-SEM graphs depicted that the involved NPs emerge in the shape of the obvious hexagonal structure, also change in crystallite size are observed with using various dopants. Dielectric and magnetic behaviors of all synthesized samples have been studied in detail through a wide frequency range of 10^{-3} Hz to 10^6 Hz at 300 K. The capacitance of the samples is decreased with frequency increasing, and also it decreases with adding Ni and Mn dopants compared with the undoped ones, which may be due to the existence of different traps that induce various time constant charges. The frequency dependence of dielectric constants is described by Maxwell–Wagner (M–W) mechanism. The increase of the imaginary part with frequency decreases is also related to the migration of ions. Nickel doping enables capacitive behavior at lower frequencies in comparison with manganese. The magnetic behavior of Ni-doped NPs is observed after its electrical behavior at higher frequency values than Mn-doped NPs. Similarly, the same proportion is observed between the order of electrical and magnetic behavior for Mn doped with respect to the pure ZnO (see Fig. 15). Dielectric loss tangent plot indicates that at higher frequencies it increases with doping which makes undoped ZnO to be a proper material for high-frequency applications and utilization in supercapacitors and batteries. Modulus graphs exhibit an increment at higher frequencies, but their values approach zero at the lower frequencies. Also, modulus values increase with doping and for Ni-doped ZnO NPs they have the greatest values. The AC conductivity measurements revealed that the conductivity decreases through doping and the lowest value belongs to the Ni-doped ZnO sample. In general, AC conductivity increases

gradually with frequency increasing which is caused by enhanced dielectric relaxation of undoped and doped ZnO samples polarization in higher frequencies and also it is relevant to the space charge polarization. With increasing frequency, magnetic loss tends to frequency-independent nature at a higher frequency. Finally, by considering the magnetic characteristic and orientation of the magnetic dipoles of nickel and manganese, it can be observed that Ni doping causes a less magnetic loss tan in comparison with Mn doping of ZnO. The same proportion is observed between the order of Mn doped with respect to pure ZnO.

References

1. A. Koo, R. Yoo, S.P. Woo, H.-S. Lee, W. Lee, *Sens. Actuators B Chem.* **280**, 109 (2019)
2. C. Madhu, I. Kaur, N. Kaur, *J. Mater. Sci.* **29**, 7785 (2018)
3. P. Meng, X. Zhao, Z. Fu, J. Wu, J. Hu, J. He, *J. Alloys Compd.* **789**, 948 (2019)
4. X. Suo, S. Zhao, Y. Ran, H. Liu, Z. Jiang, Y. Li, Z. Wang, *Surf. Coat. Technol.* **357**, 978 (2019)
5. A. Ulyankina, I. Leontyev, M. Avramenko, D. Zhigunov, N. Smirnova, *Mater. Sci. Semicond. Process.* **76**, 7 (2018)
6. V.D. Mote, Y. Purushotham, B.N. Dole, *Mater. Des.* **96**, 99 (2016)
7. S. Guo, Q. Hou, C. Zhao, Y. Zhang, *Chem. Phys. Lett.* **614**, 15 (2014)
8. R. Nasser, W.B.H. Othmen, H. Elhouichet, *Ceram. Int.* **45**, 8000 (2019)
9. B. Hartiti, M. Siadat, E. Comini, H.M.M.M. Arachchige, S. Fadili, P. Thevenin, *J. Mater. Sci.* **30**, 7681 (2019)
10. D. Sharma, R. Jha, *J. Alloys Compd.* **698**, 532 (2017)
11. N.X. Sang, N.M. Quan, N.H. Tho, N.T. Tuan, T.T. Tung, *Semicond. Sci. Technol.* **34**, 25013 (2019)
12. C. Belkhaoui, R. Lefi, N. Mzabi, H. Smaoui, *J. Mater. Sci.* **29**, 7020 (2018)
13. A. Zia, S. Ahmed, N.A. Shah, M. Anis-ur-Rehman, E.U. Khan, M. Basit, *Phys. B Condens. Matter* **473**, 42 (2015)
14. K. Ravichandran, K. Karthika, B. Sakthivel, N.J. Begum, S. Snega, K. Swaminathan, V. Senthamilselvi, *J. Magn. Magn. Mater.* **358**, 50 (2014)
15. K.P. Shinde, R.C. Pawar, B.B. Sinha, H.S. Kim, S.S. Oh, K.C. Chung, *Ceram. Int.* **40**, 16799 (2014)
16. S.M. Mousavi, A.R. Mahjoub, R. Abazari, *J. Mol. Liq.* **242**, 512 (2017)
17. S. Aksoy, Y. Caglar, *J. Alloys Compd.* **781**, 929 (2019)
18. S. Agarwal, P. Rai, E.N. Gatell, E. Llobet, F. Güell, M. Kumar, K. Awasthi, *Sens. Actuators B Chem.* **292**, 24 (2019)
19. D. Richard, M. Romero, R. Faccio, *Ceram. Int.* **44**, 703 (2018)
20. G. Vijayaprasath, R. Murugan, T. Mahalingam, G. Ravi, *J. Mater. Sci.* **26**, 7205 (2015)
21. Y. Mao, Y. Li, Y. Zou, X. Shen, L. Zhu, G. Liao, *Ceram. Int.* **45**, 1724 (2019)
22. D. Klauson, I. Gromyko, T. Dedova, N. Pronina, M. Krichevskaya, O. Budarnaja, I.O. Acik, O. Volobujeva, I. Sildos, K. Utt, *Mater. Sci. Semicond. Process.* **31**, 315 (2015)
23. H.M. Chenari, M.M. Golzan, H. Sedghi, A. Hassanzadeh, M. Talebian, *Curr. Appl. Phys.* **11**, 1071 (2011)
24. O. S. Heavens, *Thin Film Physics* (Methuen, 1970)
25. Y. Liu, H. Liu, Z. Chen, N. Kadasala, C. Mao, Y. Wang, Y. Zhang, H. Liu, Y. Liu, J. Yang, *J. Alloys Compd.* **604**, 281 (2014)

26. A.H. Bahrami, H. Ghayour, S. Sharafi, Powder Technol. **249**, 7 (2013)
27. S.O. Gashti, A. Fattah-Alhosseini, Y. Mazaheri, M.K. Keshavarz, J. Alloys Compd. **688**, 44 (2016)
28. T. Debnath, P. Saha, N. Patra, S. Das, S. Sutradhar, J. Appl. Phys. **123**, 194101 (2018)
29. G. Kafili, A. Alhaji, Adv. Powder Technol. **30**, 1108 (2019)
30. P. Shukla, J.K. Shukla, J. Supercond. Nov. Magn. **32**, 721 (2019)
31. D. Anbuselvan, S. Muthukumaran, Opt. Mater. (Amst). **42**, 124 (2015)
32. M. Robles-Águila, J. Luna-López, Á. Hernández de la Luz, J. Martínez-Juárez, M. Rabanal, Crystals **8**, 406 (2018)
33. P.K. Kannan, R. Saraswathi, J.B.B. Rayappan, Ceram. Int. **40**, 13115 (2014)
34. G. Srinet, R. Kumar, V. Sajal, J. Appl. Phys. **114**, 33912 (2013)
35. B. Manikandan, T. Endo, S. Kaneko, K.R. Murali, R. John, J. Mater. Sci. **29**, 9474 (2018)
36. R. Gopalakrishnan, S. Muthukumaran, J. Mater. Sci. **24**, 1069 (2013)
37. Y.-M. Hao, S.-Y. Lou, S.-M. Zhou, R.-J. Yuan, G.-Y. Zhu, N. Li, Nanoscale Res. Lett. **7**, 100 (2012)
38. M.F. Khan, A.H. Ansari, M. Hameedullah, E. Ahmad, F.M. Husain, Q. Zia, U. Baig, M.R. Zaheer, M.M. Alam, A.M. Khan, Sci. Rep. **6**, 27689 (2016)
39. R. Siddheswaran, M. Netrvalová, J. Savková, P. Novák, J. Očenášek, P. Šutta, J. Kováč Jr., R. Jayavel, J. Alloys Compd. **636**, 85 (2015)
40. S. Fabbiyola, V. Sailaja, L.J. Kennedy, M. Bououdina, J.J. Vijaya, J. Alloys Compd. **694**, 522 (2017)
41. A. Samanta, M.N. Goswami, P.K. Mahapatra, J. Alloys Compd. **730**, 399 (2018)
42. F. Ahmed, N. Arshi, M.S. Anwar, R. Danish, B.H. Koo, RSC Adv. **4**, 29249 (2014)
43. A. Yildiz, B. Yurduguzel, B. Kayhan, G. Calin, M. Dobromir, F. Iacomi, J. Mater. Sci. **23**, 425 (2012)
44. K. Omri, I. Najeh, L. El Mir, Ceram. Int. **42**, 8940 (2016)
45. Y. Cherifi, A. Chaouchi, Y. Lorgoilloux, M. Rguiti, A. Kadri, C. Courtois, Process. Appl. Ceram. **10**, 125 (2016)
46. A. Goswami, A.P. Goswami, Thin Solid Films **16**, 175 (1973)
47. H.M. Chenari, A. Hassanzadeh, M.M. Golzan, H. Sedghi, M. Talebian, Curr. Appl. Phys. **11**, 409 (2011)
48. F. Kremer, A. Schönhal, *Broadband Dielectric Spectroscopy* (Springer, New York, 2012)
49. A. Tataroglu, Ş. Altundal, M.M. Bülbül, Microelectron. Eng. **81**, 140 (2005)
50. I. Khan, S. Khan, W. Khan, Mater. Sci. Semicond. Process. **26**, 516 (2014)
51. M.M. El-Nahass, H.A.M. Ali, Solid State Commun. **152**, 1084 (2012)
52. A. Tabib, N. Sdiri, H. Elhouichet, M. Férid, J. Alloys Compd. **622**, 687 (2015)
53. A. Azam, A.S. Ahmed, M.S. Ansari, A.H. Naqvi, J. Alloys Compd. **506**, 237 (2010)
54. S. Khera, P. Chand, Chin. J. Phys. **57**, 28 (2019)
55. R. Khan, S. Fashu, J. Mater. Sci.: Mater. Electron. **28**, 4333 (2017)
56. M. Ashokkumar, S. Muthukumaran, J. Magn. Magn. Mater. **374**, 61 (2015)
57. D. Varshney, S. Dwivedi, Mater. Res. Express **2**, 106102 (2015)
58. M. Ashokkumar, S. Muthukumaran, J. Lumin. **162**, 97 (2015)
59. C.-H. Ho, C.-D. Liu, C.-H. Hsieh, K.-H. Hsieh, S.-N. Lee, Synth. Met. **158**, 630 (2008)
60. R. Zamiri, B. Singh, I. Bdikin, A. Rebelo, M.S. Belsley, J.M.F. Ferreira, Solid State Commun. **195**, 74 (2014)
61. M. Kaddes, K. Omri, N. Kouaydi, M. Zemzemi, Appl. Phys. A **124**, 518 (2018)
62. M.D.P. Ahmad, A.V. Rao, K.S. Babu, G.N. Rao, Mater. Chem. Phys. **224**, 79 (2019)
63. D. K. Cheng, *Field and Wave Electromagnetics* (Pearson Education India, 1989)
64. J.E. Jaffe, R. Pandey, A.B. Kunz, Phys. Rev. B **43**, 14030 (1991)
65. V. Pazhanivelu, A.P.B. Selvadurai, R. Kannan, R. Murugaraj, Phys. B Condens. Matter **487**, 102 (2016)

Publisher's Note Springer Nature remains neutral with regard to jurisdictional claims in published maps and institutional affiliations.